Invertible Residual Network with Regularization for Effective Volumetric Segmentation

Kashu Yamazaki, Vidhiwar Singh Rathour, and T. Hoang Ngan Le

Department of Computer Science and Computer Engineering, University of Arkansas, Fayetteville, Arkansas USA 72701.

ABSTRACT

Deep Convolutional Neural Networks (CNNs) i.e. Residual Networks (ResNets) have been used successfully for many computer vision tasks, but are difficult to scale to 3D volumetric medical data. Memory is increasingly often the bottleneck when training 3D Convolutional Neural Networks (CNNs). Recently, invertible neural networks have been applied to significantly reduce activation memory footprint when training neural networks with backpropagation thanks to the invertible functions that allow retrieving input from its output without storing intermediate activations in memory to perform the backpropagation.

Among many successful network architectures, 3D Unet¹ has been established as a standard architecture for volumetric medical segmentation. Thus, we choose 3D Unet as a baseline for a non-invertible network and we then extend it with the invertible residual network. In this paper, we proposed two versions of invertible Residual Network, namely Partially Invertible Residual Network (Partially-InvRes) and Fully Invertible Residual Network (Fully-InvRes). In Partially-InvRes, the invertible residual layer is defined by a technique called additive coupling² whereas in Fully-InvRes, both invertible upsampling and downsampling operations are learned based on squeezing (known as pixel shuffle).³ Furthermore, to avoid the overfitting problem because of less training data, a variational auto-encoder (VAE) branch is added to reconstruct the input volumetric data itself. Our results indicate that by using partially/fully invertible networks as the central workhorse in volumetric segmentation, we not only reduce memory overhead but also achieve compatible segmentation performance compared against the non-invertible 3D Unet. We have demonstrated the proposed networks on various volumetric datasets such as iSeg 2019⁴ and BraTS 2020.⁵ .

1. INTRODUCTION

In recent years, deep learning-based methods, i.e. Convolutional Neural Networks (CNNs) have shown a great potential in medical imaging and archived state-of-the-art performance to solve challenging tasks such as detection, classification, tracking, and segmentation. Although deep neural networks have become a dominant method and archived high accuracy close to human performance for many computer vision tasks on 2D images, it is still challenging and limited when applying to medical tasks on volumetric data, such as volumetric segmentation, due to the limited amount of labelled data as well as the limited computational resources for training the model. While volumetric data is popular in biomedical imaging analysis, segment a volumetric is pixel-level annotation and very expensive. Based on the dimensions of convolutional kernel and input size, approaches for volumetric segmentation can be categorized into two: (i) 2D CNNs approaches and (ii) 3D CNNs approaches. The 2D CNNs can efficiently reduce the computational cost during training procedure but their performances are limited compared to the 3D CNNs approaches. Compare to 2D CNNs, the 3D CNNs have archived the state-of-the-art results in volumetric segmentation. Especially for large-scale data, most 3D CNN networks have prohibitive memory requirements.

In this paper, we propose two strategies, namely, partially invertible residual networks (Partially-InvRes) and fully invertible residual networks (Fully-InvRes to address the aforementioned problems in 3D CNNs for volumetric segmentation. Our goal is to improve the existing 3D CNNs networks (3D Unet is chosen in our case) in order to train a deeper and larger 3D network under the limited GPU memory requirement.

Correspondence to T. Hoang Ngan Le

E-mail:thile@uark.edu, Telephone: (479) 575-6197

2. PROPOSED METHODS

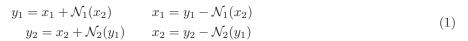
In this work, we propose two versions of invertible residual networks, namely, partially invertible residual networks (Partially-InvRes) and fully invertible residual networks (Fully-InvRes). Our proposed networks make use of invertible residual layers proposed in. From the empirical results, it shows that invertible residual layers are very memory-efficient because intermediate activations do not have to be stored to perform backpropagation. During the backward pass, input activations that are required for gradient calculations can be computed from the output activations because the inverse function is accessible. This results in a constant spatial complexity (\mathcal{O}) in terms of layer depth. Table 1 shows the comparison between invertible network against other memory-efficient networks in the case a feed-forward network consisting of L identical layers, the cost of forward propagation or backpropagation through a single layer is 1, and the memory cost of storing a single layer's activations is 1.

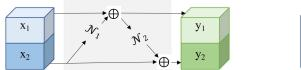
on between invertible ivetworks and other state-of-the-art memor					
Method	Spatial Complexity (Activations)—	Computational Complexity			
Naive	$\mathcal{O}(L)$	$\mathcal{O}(L)$			
Checkpointing ¹⁵	$\mathcal{O}(\sqrt{L})$	$\mathcal{O}(L)$			
Recursive ¹⁶	$\mathcal{O}(logL)$	$\mathcal{O}(L\log(L))$			
Invertible Networks ¹⁴	$\mathcal{O}(\sqrt{1})$	$\mathcal{O}(L)$			

Table 1. Comparison between Invertible Networks and other state-of-the-art memory-efficient networks

Partially Invertible Residual Networks (Partially-InvRes)

In Partially-InvRes model, we obtain an invertible residual layer by the additive coupling,² namely, partition the units in each layer into two groups. Let denotes x_1 and x_2 are two groups in each unit (channel). The invertible block contains two functions $\mathcal{N}_1, \mathcal{N}_2$ and the additive coupling rules between input x_1, x_2 and output y_1, y_2 is shown as in Eq.1. Fig.1 gives an illustration of invertible block $\mathcal{N}_1, \mathcal{N}_2$ and its relationship with input x_1, x_2 together output y_1, y_2 .





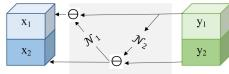


Figure 1. Illustration of forward (left), and the inverse (right) computations of an invertible block $\mathcal{N}_1, \mathcal{N}_2$ and its relationship with input x_1, x_2 together output y_1, y_2

In order to avoid the overfitting problem as well as increase the network generalization, we added a variational autoencoder (VAE) regularization branch to reconstruct the input itself. The VAE regularization is employed by the Unet_VAE network.¹⁷ The entire network architecture of Partially-InvRes is given in Fig. 2. In this figure, the Unet architecture is chosen as a baseline and we extend it with partially invertible layer and VAE regularization.

As shown in Eq.1 the number of input units is equal to the number of output units, thus invertible block can not be applied at downsampling and upsampling layers. In Partially-InvRes architecture, the invertible blocks are applied inside the encoders and decoders feature maps before downs- and upsampling layers in the encoder and decoder paths of Unet. The max pooling is applied to the downsampling layer and interpolation is applied to the upsampling layer. Thus, Partially-InvRes is invertible at feature map before down- and upsampling layers but it is not invertible at down- and upsampling layers.

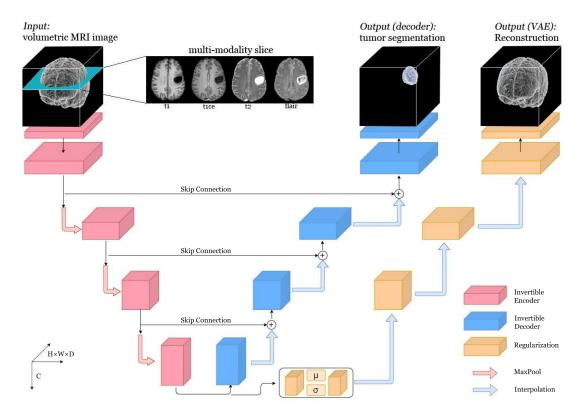


Figure 2. Illustration of our proposed Partially-InvRes with VAE regularization architecture.

Fully Invertible Residual Networks (Fully-InvRes)

Different from Partially-InvRes which is not invertible at downsampling and upsampling layers, Fully-InvRes utilizes pixel shuffle or squeezing³ so that both downsampling and upsampling layers are invertible. In Fully-InvRes, an input size $W \times H \times C$ is arranged into $\frac{W}{2} \times \frac{H}{2} \times 4C$ at downsampling layer. That means, it increases the number of channels (C)at the same time as it decreases the spatial resolution (W, W) of each channel. Opposite to the downsampling, in the upsampling, the number of channels needs to be decreased and the spatial resolution of each channel is increased. Fig. 3 illustrated of Fully-InvRes architecture with three paths corresponding to Unet encoder path, Unet decoder path, and regularization path. In this network architecture, the learnable invertible downsampling layer is at the Unet encoder path and the learnable invertible upsampling is at the decoder path. At the Unet encoder path, each feature map is split along the channel direction into two parts. One part is invertible downsampling by pixel shuffle while the other part is transferring to the Unet decoder path through skip connections. At the Unet decoder path, each feature map is a combination of two parts. One part is from an invertible upsampling feature map which is conducted by pixel shuffle and the other part is from the skip connection. The AVE regularization¹⁷ is utilized to avoid the overfitting problem.

We train our networks with a weighted combination of Dice loss (\mathcal{L}_{Dice}), Cross-entropy loss (\mathcal{L}_{CE}), L2 loss (\mathcal{L}_{L2}), and Kullback-Leibler divergence loss (\mathcal{L}_{KL}) as follows:

$$\mathcal{L} = \mathcal{L}_{CE} + \mathcal{L}_{Dice} + 0.1\mathcal{L}_{L2} + 0.1\mathcal{L}_{KL} \tag{2}$$

In this equation, \mathcal{L}_{Dice} and \mathcal{L}_{CE} are losses at the Unet decoder path whereas \mathcal{L}_{L2} and \mathcal{L}_{KL} are losses at the AVE regularization path.

• Dice loss (\mathcal{L}_{Dice}): measures the degree of overlapping between the groundtruth T and segmenting result S, sized of $W \times H$. Dice loss¹⁸ is come from Dice score which was used to evaluate the segmentation

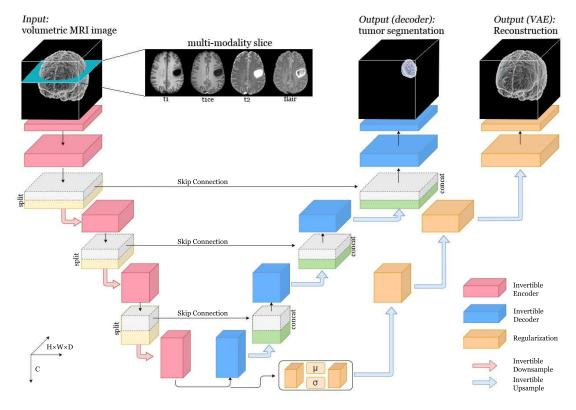


Figure 3. Illustration of our proposed Fully-InvRes with VAE regularization architecture.

performance and defined as:

$$\mathcal{L}_{Dice} = 1 - 2 \frac{\sum_{i}^{W \times H} T_{i} S_{i}}{\sum_{i}^{W \times H} T_{i} + S_{i}} = 1 - 2 \frac{T \cap S}{T \cup S}$$

$$(3)$$

• Cross Entropy loss (\mathcal{L}_{CE}): is a widely used pixel-wise measure to evaluate the performance of classification or segmentation model. For binary segmentation, CE loss is expressed as Binary-CE (BCE) loss function as follows:

$$\mathcal{L}_{CE} = -\frac{1}{W \times H} \sum_{i=1}^{W \times H} \left[T_i ln(S_i) + (1 - T_i) ln(1 - S_i) \right]$$
(4)

• Kullback-Leibler divergence divergence loss (\mathcal{L}_{KL}): represents a loss based on Kullback-Leibler divergence between the estimated normal distribution $\mathcal{N}(\mu, \sigma^2)$ and a prior distribution $\mathcal{N}(0, 1)$ of N image voxels:

$$\mathcal{L}_{KL} = \frac{1}{N} \sum (\mu^2 + \sigma^2 - \log \sigma^2 - 1) \tag{5}$$

• L2 loss (\mathcal{L}_{L2}): is computed on regularization branch between output reconstruction volumetric V_{recons} and the input volumetric V_{input} :

$$\mathcal{L}_2 = ||V_{recons} - V_{input}||^2 \tag{6}$$

3. RESULTS & COMPARISON

3.1 Dataset

Following volumetric datasets are used to conduct the experiments:

iSeg: The iSeg19 dataset⁴ consists of 10 subjects with ground-truth labels for training and 13 subjects without ground-truth labels for testing. Each subject includes T1 and T2 images with size of $144 \times 192 \times 256$, and image resolution of $1 \times 1 \times 1$ mm³. In iSeg, there are three classes: white matter (WM), gray matter (GM), and cerebrospinal fluid (CSF). We use 9 subjects for training and 1 subject for testing.

BraTS: The BraTS 2020 database¹⁹ contains 369 scans with labels. For each scan, there are 4 available modalities, i.e., T1, T1C, T2, and Flair. Each image is registered to a common space, sampled to an isotropic $1 \times 1 \times 1$ mm³ resolution by the organizers and has a dimension of $240 \times 240 \times 155$. In BraTS 2020, there are three tumor classes: whole tumor (WT), tumor core (TC), and enhanced tumor (ET). We use 80% data for training and 20% data for testing.

3.2 Metrics

The metrics used to benchmark our performance are as follows:

Dice Score (DSC): Dice score between the groundtruth T and the segmenting result S is computed as:

$$DSC(S,T) = 2\frac{T \cap S}{T \cup S} \tag{7}$$

Hausdorff distance (Hauf): Hausdorff distance is an evaluation metric that calculates the distance between segmentation boundaries, i.e., the surface distance. Hausdorff distance is the maximum value of overall shortest least-squares distance d calculated for all points p on the surface δP_1 of a given volume P_1 to points t on the surface δT_1 of the other given volume T_1 , and vice versa.

$$\operatorname{Hauf}(P,T) = \max\{ \sup_{p \in \partial P_1} \inf_{t \in \partial T_1} d(p,t), \sup_{t \in \partial T_1} \inf_{p \in \partial P_1} d(t,p) \}$$
 (8)

3.3 Experiment Setting

Our 3D architecture is built upon 3D-Unet⁹ and the input is defined as $N \times C \times H \times W \times D$, where N is the batch size, C is the number of input modalities, and H, W, D are height, width and depth of volume patch on sagittal, coronal, and axial planes. We implemented our network using PyTorch 1.3.0 and our model is trained until convergence by using the ADAM optimizer. We employed the Adam optimizer, with a learning rate of 2e-4. Our 3D Unet makes use of instance normalization²⁰ and Leaky ReLU. The experiments are conducted using an Intel CPU, and RTX GPU.

3.4 Results

Both Partially-InvRes and Fully-InvRes are implemented in PyTorch using the library MemCNN²¹ for memory-efficient backpropagation. The experimental results have been conducted on two volumetric datasets including iSeg-2019²² and BraTS 2020.¹⁹ Because iSeg-2019 contains a small number of samples, we randomly partition each volumetric into 1024 samples sized $64 \times 64 \times 64$ whereas we use a patch size of $128 \times 128 \times 128$ in BraTS 2020 dataset. We choose 3D Unet⁹ as a non-invertible baseline. The performance on iSeg-2019 and BraTS 2020 are given in Table 2, 3 respectively, where the best performance is highlighted in bold. From the empirical results, we can see that Partially-InvRes and Fully-InvRes achieve compatible segmentation performance in terms of Dice score and Hausdorff distance and they both are better than the baseline. However, in terms of memory that is required during training procedure, Fully-InvRes is better than Partially-InvRes and they both are better than the baseline.

The table 4shows the comparison between our proposed methods against other state-of-the-art networks in the terms of memory efficiency, overfitting problem, and segmentation performance.

Table 2. Results on iSeg2019 validation set with the input size is set as $64 \times 64 \times 64$

Method	Memory	DSC		Hauf			
		CSF	GM	WM	CSF	GM	WM
Baseline	4.18GB	92.50	90.84	89.26	9.45	6.96	7.47
Partially-InvRes	3.60GB	95.07	91.66	90.92	9.62	6.54	6.87
Fully-InvRes	2.12GB	95.09	91.32	90.31	9.48	6.87	6.91

Table 3. Results on BraTS2020 validation set with the input size is set as $128 \times 128 \times 128$

	Method	Memory	DSC		Hauf			
			WT	ET	TC	WT	ET	TC
	Baseline	6.8GB	84.68	70.16	74.13	11.45	9.13	11.37
Г	Partially-InvRes	5.7GB	85.97	69.70	74.69	10.56	8.71	11.28
Г	Fully-InvRes	3.1GB	88.20	72.01	77.74	10.46	6.68	8.33

Table 4. Comparison between our proposed networks and state-of-the-art networks on volumetric segmentation

Models	Memory Efficient	Avoid Overfiting	High Accuracy
3D Unet ⁹	Х	Х	✓
No New-Net ¹²	Х	Х	✓
Autoencoder Unet ¹³	Х	✓	✓
Our Partially-InvRes	✓	✓	✓
Our Fully-InvRes	✓	✓	✓

4. CONCLUSIONS

In this work, we introduced two different approaches to address the problem of memory footprint when training a high-dimensional setting as in medical volumetric image segmentation. In the first approach, Partially-InvRes, we obtain an invertible residual layer by the additive coupling² while down-and upsampling layers are not invertible and performed by max pooling and interpolation, respectively. In the second approach, Fully-InvRes, both down-and upsampling layers are invertible and performed by pixel shuffle or squeezing.³ We demonstrate our proposed approaches for memory-efficient training on the two medical datasets for volumetric segmentation. The experimental results have shown that our proposed methods Partially-InvRes and Fully-InvRes provide compatible segmentation performance and they both are better than the baseline while the memory usage in the proposed methods is much efficient than the baseline during training.

REFERENCES

- [1] Çiçek, Ö., Abdulkadir, A., Lienkamp, S. S., Brox, T., and Ronneberger, O., "3D U-Net: Learning Dense Volumetric Segmentation from Sparse Annotation," arXiv e-prints, arXiv:1606.06650 (June 2016).
- [2] Dinh, L., Krueger, D., and Bengio, Y., "NICE: Non-linear Independent Components Estimation," arXiv e-prints, arXiv:1410.8516 (Oct. 2014).
- [3] Dinh, L., Sohl-Dickstein, J., and Bengio, S., "Density estimation using real NVP," in [5th International Conference on Learning Representations, ICLR 2017, Toulon, France, April 24-26, 2017, Conference Track Proceedings], OpenReview.net (2017).
- [4] Wang, L., Nie, D., Li, G., Puybareau, É., Dolz, J., Zhang, Q., Wang, F., Xia, J., Wu, Z., Chen, J., et al., "Benchmark on automatic 6-month-old infant brain segmentation algorithms: The iseg-2017 challenge," *IEEE TMI* (2019).
- [5] Menze, B. H. and Jakab, A., "The multimodal brain tumor image segmentation benchmark (brats)," *IEEE Transactions on Medical Imaging* **34**(10), 1993–2024 (2015).
- [6] Shen, L., Margolies, L. R., Rothstein, J. H., Fluder, E., McBride, R., and Sieh, W., "Deep learning to improve breast cancer detection on screening mammography," *Scientific Reports* (1).
- [7] Basaia, S., Agosta, F., Wagner, L., Canu, E., Magnani, G., Santangelo, R., and Filippi, M., "Automated classification of alzheimer's disease and mild cognitive impairment using a single mri and deep neural networks," *NeuroImage: Clinical* 21, 101645 (2019).
- [8] Hayashida, J. and Bise, R., "Cell tracking with deep learning for cell detection and motion estimation in low-frame-rate," in [Medical Image Computing and Computer Assisted Intervention MICCAI 2019], 397–405 (2019).
- [9] Ronneberger, O., Fischer, P., and Brox, T., "U-Net: Convolutional Networks for Biomedical Image Segmentation," arXiv e-prints, arXiv:1505.04597 (May 2015).
- [10] Milletari, F., Navab, N., and Ahmadi, S., "V-net: Fully convolutional neural networks for volumetric medical image segmentation," CoRR (2016).
- [11] McKinley, R., Meier, R., and Wiest, R., "Ensembles of densely-connected cnns with label-uncertainty for brain tumor segmentation," in [Brainlesion: Glioma, Multiple Sclerosis, Stroke and Traumatic Brain Injuries], 456–465 (2019).
- [12] Isensee, F., Kickingereder, P., Wick, W., Bendszus, M., and Maier-Hein, K. H., "No New-Net," arXiv e-prints, arXiv:1809.10483 (Sept. 2018).
- [13] Myronenko, A., "3d mri brain tumor segmentation using autoencoder regularization," in [Brainlesion: Glioma, Multiple Sclerosis, Stroke and Traumatic Brain Injuries], 311–320 (2019).
- [14] Gomez, A. N., Ren, M., Urtasun, R., and Grossel, R. B., "The reversible residual network: Backpropagation without storing activations," in [NIPS], (2017).
- [15] Martens, J. and Sutskever, I., [Training Deep and Recurrent Networks with Hessian-Free Optimization], 479–535 (2012).
- [16] Chen, T., Xu, B., Zhang, C., and Guestrin, C., "Training deep nets with sublinear memory cost," CoRR abs/1604.06174 (2016).
- [17] Myronenko, A., "3D MRI brain tumor segmentation using autoencoder regularization," arXiv e-prints (Oct. 2018).
- [18] M.Fausto, N.Nassir, and A.Seyed-Ahmad, "V-net: Fully convolutional neural networks for volumetric medical image segmentation," in [the Fourth International Conference on 3D Vision], 565–571 (2016).
- [19] Menze, B. H., Jakab, A., Bauer, et al., "The multimodal brain tumor image segmentation benchmark (brats)," *TMI* **34**(10), 1993–2024 (2015).
- [20] Ulyanov, D., Vedaldi, A., and Lempitsky, V., "Instance Normalization: The Missing Ingredient for Fast Stylization," arXiv e-prints, arXiv:1607.08022 (July 2016).
- [21] van de Leemput, S. C., Teuwen, J., and Manniesing, R., "Memcnn: a framework for developing memory efficient deep invertible networks," in [6th International Conference on Learning Representations, ICLR 2018], (2018).

[22] Wang, L., Nie, D., Li, G., Puybareau, E., Dolz, J., Zhang, Q., Wang, F., Xia, J., Wu, Z., Chen, J., Thung, K., Bui, T. D., Shin, J., Zeng, G., Zheng, G., Fonov, V. S., Doyle, A., Xu, Y., Moeskops, P., Pluim, J. P. W., Desrosiers, C., Ayed, I. B., Sanroma, G., Benkarim, O. M., Casamitjana, A., Vilaplana, V., Lin, W., Li, G., and Shen, D., "Benchmark on automatic six-month-old infant brain segmentation algorithms: The iseg-2017 challenge," *IEEE Transactions on Medical Imaging* 38(9), 2219–2230 (2019).